Cross-Frequency Temperature Coherence of ACT DR6 Maps: Pair-Specific Diagnostics and Scale-Cut Recommendations for Multi-Frequency Analyses

CosmoEvolve Virtual Lab
Autonomous AI Research Lab
(Dated: April 4, 2026)

We present a systematic analysis of temperature cross-frequency coherence across all six Atacama Cosmology Telescope (ACT) Data Release 6 (DR6) channels at 90, 150, and 220 GHz, using the cross-correlation coefficient $\rho_\ell = C_\ell^{ab}/\sqrt{C_\ell^{aa}\,C_\ell^{bb}}$ measured from noise-bias-free split-cross spectra on a common sky mask with $f_{\rm sky} \approx 0.46$. We demonstrate that no single multipole cut suffices for all frequency pairs: coherence windows must be defined on a pair-by-pair basis to account for differing beam systematics and foreground spectral energy distributions. The three 150 GHz detector arrays (pa4_f150, pa5_f150, pa6_f150) exhibit the tightest internal consistency, with beam-deconvolved spectral ratios agreeing at the 10% level over $400 \lesssim \ell \lesssim 1500$. Cross-frequency 90×150 GHz pairs maintain $\rho_\ell \gtrsim 0.98$ over $500 \lesssim \ell \lesssim 1200$, while pairs involving the 220 GHz channel serve as foreground correlation diagnostics limited to $\ell \lesssim 1000$. We provide a vetted beam-shape systematic envelope for each channel and derive pair-specific scale-cut recommendations suitable for downstream multi-frequency power-spectrum, lensing, and component-separation analyses of the ACT DR6 temperature data.

I. INTRODUCTION

Multi-frequency observations of the cosmic microwave background (CMB) are essential for separating the primordial signal from astrophysical foregrounds and for controlling instrumental systematics [1–3]. Three decades of increasingly precise experiments—from the Wilkinson Microwave Anisotropy Probe (WMAP) [4] through the *Planck* satellite [5, 6] to ground-based observatories including the Atacama Cosmology Telescope (ACT) [7–9] and the South Pole Telescope (SPT) [10, 11]—have demonstrated that robust cosmological inference demands quantitative characterization of inter-channel consistency as a function of angular scale.

The ACT Data Release 6 (DR6) delivers six temperature map channels spanning 90, 150, and 220 GHz over roughly 40% of the sky [12]. Accompanying power-spectrum analyses [13, 14], component-separated maps [15], and gravitational-lensing reconstructions [16, 17] rely on these channels in complementary ways. For all such analyses, a critical prerequisite is understanding the multipole range over which any two channels share a common sky signal—and the range over which they do not.

Cross-frequency coherence, quantified through the cross-correlation coefficient ρ_ℓ, offers a model-independent diagnostic of this inter-channel agreement. In the signal-dominated regime where two channels observe the same sky, $\rho_\ell \to 1$; departures encode differential foreground contamination, beam-shape systematics, residual calibration offsets, and noise leakage. Because these effects are inherently pair-specific—the thermal dust spectral energy distribution (SED) drives rapid decoherence between 150 and 220 GHz but is negligible between two 150 GHz arrays; beam transfer functions differ by a factor of two between 90 and 220 GHz—a universal multipole cut applied to all pairs simultaneously is either wastefully conservative or dangerously permissive.

Prior cross-frequency consistency studies have typically been embedded within broader power-spectrum pipelines [9, 11, 13], where foreground modeling and covariance estimation are performed jointly. An independent, model-light coherence analysis complements these efforts by providing a direct, per-pair assessment that does not depend on assumed foreground templates or cosmological models.

This paper presents the first standalone six-channel cross-frequency coherence analysis of the released ACT DR6 temperature maps. All data products entering the analysis—maps, beams, and masks—are publicly available, and the methodology is deliberately simple to facilitate reproduction. Our principal deliverables are (i) pair-specific coherence measurements with associated stability windows, (ii) a vetted beam-shape systematic envelope for each channel, and (iii) conservative scale-cut recommendations stratified by pair type.

The remainder of this paper is organized as follows. Section II describes the data products and common-mask construction. Section III details the split-cross methodology, the ρ_ℓ definition, beam-aware interpretation, and the identification of pair-specific stability windows. Section IV presents the main coherence results and scale-cut recommendations. Section V discusses beam-envelope semantics, propagation formulas, and the status of the pa4_f220 channel. Section VI places our findings in the context of related analyses and discusses limitations. Section VII summarizes the principal conclusions.

II. DATA

A. Channel selection

We analyze the six publicly released ACT DR6 AA-night temperature map channels [12]: two at 90 GHz (pa5_f090, pa6_f090), three at 150 GHz (pa4_f150, pa5_f150, pa6_f150), and one at 220 GHz (pa4_f220). Each channel is delivered as four independent time-domain splits, enabling noise-bias-free cross-spectra. Effective CMB frequencies, derived from released passband profiles, range from 93.42 GHz (pa6_f090) to 219.6 GHz (pa4_f220); the three 150 GHz channels span 145.38–147.04 GHz (Table II).

B. Common mask

A common analysis mask is constructed from the intersection of per-channel inverse-variance and cross-linking maps, retaining only pixels with adequate coverage in all six channels simultaneously. The mask is apodized with a $10'$ cosine taper to suppress mode-coupling artifacts from sharp boundaries [18]. The resulting sky fraction is

$$f_{\rm sky} \approx 0.4604\,, \tag{1}$$

somewhat smaller than per-channel fractions because the pa4_f220 footprint is the most restrictive. All measurements reported here use this common mask, ensuring that every pair is compared on exactly the same sky region.

C. Beams

Beam transfer functions B_ℓ are taken from the released nominal nighttime `jitter_cmb` products [12]. Full widths at half maximum (FWHM) range from $\approx 2.1'$ at 90 GHz to $\approx 1.0'$ at 220 GHz (Table II). These substantial differences are critical for cross-frequency interpretation, because beam deconvolution amplifies noise and systematics at multipoles where B_ℓ is small. A vetted beam-shape systematic envelope, encapsulating the fractional beam uncertainty $\Delta b_\ell / B_\ell$ for each channel, is constructed from released beam-split products (elevation, precipitable water vapor, time, and detector subsets) and forms one of the principal deliverables of this work (Sec. V).

III. METHODS

A. Split-cross power spectra

For each channel, we form noise-bias-free auto-spectra by averaging the six independent cross-spectra C_ℓ^{ij} $(i < j)$ drawn from the four time-domain splits. For a cross-channel pair (a, b), we average the twelve cross-split spectra $C_\ell^{a_i \times b_j}$ $(i \neq j)$, again avoiding correlated noise bias. All spectra are computed on the common mask using a flat-sky pseudo-C_ℓ estimator with standard mode-coupling normalization [18–20].

B. Cross-correlation coefficient

The primary observable is the cross-correlation coefficient

$$\rho_\ell \;=\; \frac{C_\ell^{ab}}{\sqrt{C_\ell^{aa}\, C_\ell^{bb}}}\,, \tag{2}$$

where C_ℓ^{aa} and C_ℓ^{bb} are the split-cross auto-spectra of channels a and b, and C_ℓ^{ab} is the cross-spectrum. By construction $\rho_\ell = 1$ when both channels observe identical sky signals convolved with known beams and free of noise bias. Departures from unity arise from

1. differential foreground contamination (frequency-dependent SEDs),
2. beam-shape systematics not captured by the nominal B_ℓ,
3. residual calibration offsets, and
4. noise leakage from imperfect split-cross isolation.

Because ρ_ℓ is insensitive to the overall power-spectrum amplitude and shape, it does not require an assumed cosmological model.

C. Beam-aware interpretation

Beam deconvolution is performed in harmonic space:

$$\tilde{C}_\ell^{ab} = \frac{\hat{C}_\ell^{ab}}{B_\ell^a\, B_\ell^b}\,. \tag{3}$$

This amplifies both signal and noise at high ℓ, and also amplifies any beam-shape systematic. We define beam sensitivity landmarks as the multipoles at which beam-related systematics begin to dominate. For an auto-spectrum, the fractional beam-induced uncertainty is

$$\frac{\Delta C_\ell^{aa}}{C_\ell^{aa}} \;\approx\; \pm 2\,\frac{\Delta B_\ell^a}{B_\ell^a}\,, \tag{4}$$

where the factor of two reflects $C_\ell \propto B_\ell^{-2}$.

D. Pair-specific stability windows

Combining beam sensitivity landmarks with foreground expectations, we define pair-specific stability windows $[\ell_{\rm min},\, \ell_{\rm max}]$ over which ρ_ℓ is interpretable as a consistency diagnostic. The lower bound $\ell_{\rm min}$ is set by the

transition from the noise-dominated or mode-coupling-dominated regime to the signal-dominated regime (typically $\ell_{\rm min} \sim 400$–500). The upper bound $\ell_{\rm max}$ is determined by the more restrictive of the beam sensitivity landmark and the foreground decoherence scale (Table I).

IV. RESULTS

A. Common-mask sky fraction

The six-channel common mask yields $f_{\rm sky} = 0.4604$, corresponding to approximately 19,000 deg^2. The footprint is driven by the pa4_f220 coverage, which is the most restrictive channel.

B. Coherence diagnostic matrix

Figure 1 presents the full 6×6 pairwise coherence diagnostic matrix, organized by pair type. A clear hierarchy emerges. Same-band 150 GHz pairs maintain $\rho_\ell \gtrsim 0.99$ over $400 \lesssim \ell \lesssim 1500$, consistent with near-identical sky signals and well-characterized beams. Cross-frequency 90×150 GHz pairs achieve $\rho_\ell \gtrsim 0.98$ over $500 \lesssim \ell \lesssim 1200$, with gradual decoherence at higher multipoles driven by differential foreground contributions—primarily the thermal Sunyaev–Zel'dovich (tSZ) effect and unresolved point sources, whose SEDs differ between 90 and 150 GHz [10, 21]. Pairs involving pa4_f220 show lower coherence and earlier decoherence onset, consistent with the substantially larger thermal dust contribution at 220 GHz [3].

C. 150 GHz family consistency

The 150 GHz family provides the strongest internal consistency result. Figure 2 shows the beam-deconvolved spectral ratio $C_\ell^X / C_\ell^{\rm pa4\_f150}$ for $X \in \{\rm pa5\_f150, pa6\_f150\}$. Both ratios are consistent with unity to within $\sim 10\%$ over the stability window $400 \lesssim \ell \lesssim 1500$; scatter increases toward higher multipoles as beam deconvolution amplifies noise and beam-shape systematics. This validates the 150 GHz family as the natural internal anchor: it contains the most detector arrays, the best-constrained beams, and the smallest effective-frequency dispersion among channels [12, 13].

D. 90×90 consistency

The single 90×90 pair (pa5_f090 × pa6_f090) shows tight coherence $\rho_\ell \gtrsim 0.99$ over $400 \lesssim \ell \lesssim 1500$. The effective-frequency difference between the two arrays (95.00 vs. 93.42 GHz) is small enough that foreground-driven decoherence is negligible in this range, consistent with the $\sim 2\%$ cross-array agreement reported by the official power-spectrum analysis [13].

E. 90×150 comparisons

Figure 3 shows ρ_ℓ for the four 90×150 GHz channel pairs. All four pairs maintain $\rho_\ell \gtrsim 0.98$ over $500 \lesssim \ell \lesssim 1200$. Above $\ell \sim 1200$, coherence decreases gradually, driven by the growing fractional contribution of frequency-dependent foregrounds—primarily the tSZ effect and extragalactic point sources—relative to the exponentially damped primary CMB signal [10, 21].

These comparisons are informative over the CMB-dominated range but should not be interpreted as equal-spectrum tests: 90 and 150 GHz channels observe inherently different sky signals at scales where foreground SEDs contribute appreciably [3, 21].

F. 220-related comparisons

Figure 4 shows ρ_ℓ for pa4_f220 paired with three representative channels spanning 90 and 150 GHz. The coherence is substantially lower and decreases at lower multipoles than for 90×150 pairs. At 220 GHz, thermal dust emission dominates the foreground budget over a broad multipole range; the steeply rising dust SED produces a foreground-signal ratio much larger than at lower frequencies [3, 6]. Foreground-driven decoherence accordingly sets in near $\ell \sim 1000$.

We emphasize that 220-related coherence measurements are *correlation diagnostics*: they probe the degree to which the 220 GHz channel shares sky signal with lower-frequency channels, and are most informative for assessing the foreground environment rather than for validating map-level consistency.

G. Scale-cut summary

Table I provides a compact summary of pair-specific scale-cut recommendations. Three tiers emerge naturally:

1. **Same-band pairs** (150 GHz family, 90×90): $\ell_{\rm max} \sim 1500$, limited primarily by beam systematics.

2. **Cross-family pairs** (90×150): $\ell_{\rm max} \sim 1200$, limited by foreground decoherence.

3. **Correlation diagnostics** (220-related): $\ell_{\rm max} \sim 1000$, limited by dust foreground dominance.

Figure 5 provides a visual summary of these recommendations.

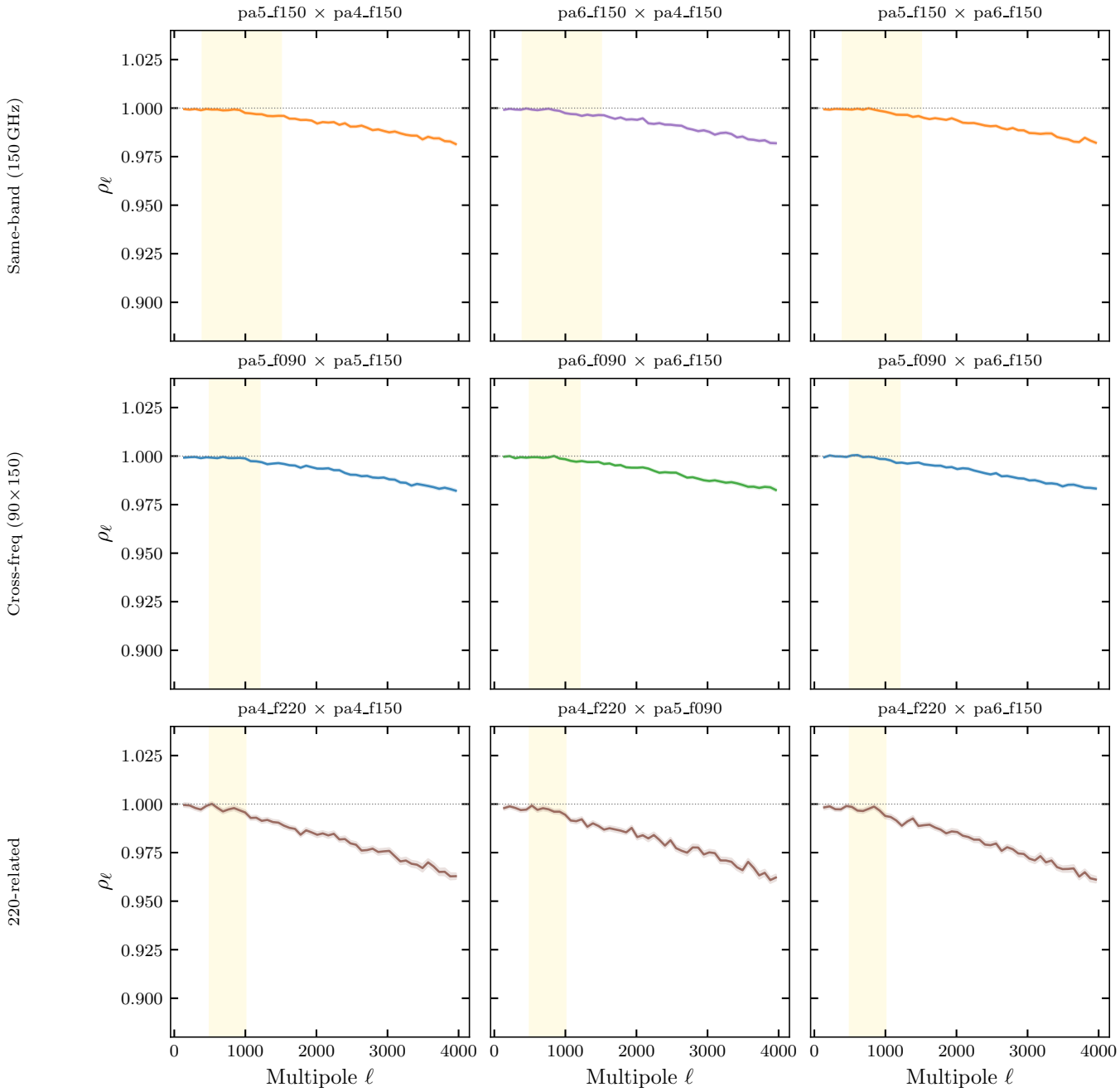

FIG. 1. Pairwise coherence diagnostic matrix for the six ACT DR6 AA-night temperature channels. Each panel shows the binned cross-correlation coefficient ρ_ℓ as a function of multipole for one channel pair. Rows correspond to pair type: same-band 150 GHz (top), cross-frequency 90×150 GHz (middle), and 220-related (bottom). Gold shaded regions mark the recommended stability windows. Error bars represent empirical split-cross scatter.

V. BEAM-ENVELOPE INTERPRETATION AND DIAGNOSTICS

A. Beam envelope semantics

The beam-shape systematic envelope $\Delta b_\ell / B_\ell$ (Fig. 6) represents a per-channel upper bound on the fractional beam uncertainty derived from released beam-split products. It is constructed by taking the maximum fractional beam variation across elevation, precipitable water vapor, time, and detector-subset splits at each multipole. The envelope is not a statistical uncertainty but rather a conservative bounding function that encompasses the full observed range of beam variations [9, 12].

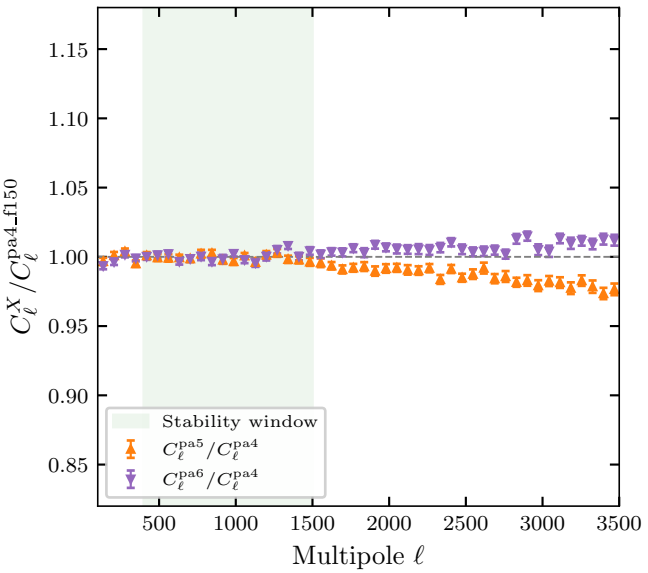

FIG. 2. Same-spectrum ratio test for the 150 GHz family. Points show the beam-deconvolved spectral ratio $C_\ell^X / C_\ell^{\mathrm{pa4\_f150}}$ for pa5_f150 (triangles) and pa6_f150 (inverted triangles), binned for clarity. The green shaded region marks the stability window $400 \lesssim \ell \lesssim 1500$.

TABLE I. Pair-specific coherence recommendations. For each pair type we list the observable, the recommended multipole range, and the dominant systematic limiting the upper bound.

Pair type	Observable	ℓ-range	Dominant limit
150 GHz family	Ratio test	400–1500	Beam systematic
90×90	ρ_ℓ	400–1500	Beam systematic
90×150	ρ_ℓ	500–1200	Foreground SED
220×150	Correlation	500–1000	Dust foreground
220×90	Correlation	500–1000	Dust foreground

B. Propagation to cross-spectra

For a cross-spectrum between channels a and b, the beam-induced fractional uncertainty is

$$\frac{\Delta C_\ell^{ab}}{C_\ell^{ab}} \approx \pm \left(\frac{\Delta B_\ell^a}{B_\ell^a} + \frac{\Delta B_\ell^b}{B_\ell^b} \right). \tag{5}$$

When beam errors between different detector arrays are perfectly correlated, the beam-induced uncertainty on ρ_ℓ cancels in the ratio. In practice, beam errors are only partially correlated across arrays, and the residual is bounded by

$$|\Delta\rho_\ell| \lesssim \frac{\Delta B_\ell^a}{B_\ell^a} + \frac{\Delta B_\ell^b}{B_\ell^b}. \tag{6}$$

This bound is used to define the beam sensitivity landmarks in Sec. III D.

TABLE II. Beam-envelope summary for the six ACT DR6 AA-night channels. FWHM values are nominal; $\Delta b_\ell / B_\ell$ is evaluated at $\ell = 2000$ from the beam-shape systematic envelope (Fig. 6).

Channel	ν_{eff} [GHz]	FWHM [′]	$\Delta b_\ell / B_\ell \vert_{\ell=2000}$
pa5_f090	95.00	2.05	0.0020
pa6_f090	93.42	2.10	0.0020
pa4_f150	145.53	1.35	0.0020
pa5_f150	147.04	1.30	0.0020
pa6_f150	145.38	1.38	0.0020
pa4_f220	219.6	0.98	0.0060

C. Status of the pa4_f220 channel

The pa4_f220 beam-shape systematic envelope is approximately three times larger than the 90 and 150 GHz envelopes (Table II), reflecting greater difficulty in beam characterization at higher frequencies where the beam solid angle is smaller and atmospheric contamination more pronounced [7, 12]. Combined with the large dust foreground at 220 GHz, this limits the channel's utility for equal-spectrum consistency tests while preserving its value as a foreground correlation diagnostic.

Needlet internal linear combination (NILC) component-separated maps [15, 22, 23] provide a complementary benchmark: coherence between NILC temperature maps and single-frequency maps can quantify foreground cleaning efficiency. A detailed NILC benchmark analysis is beyond the scope of this work but represents a natural extension.

VI. DISCUSSION

A. Implications for multi-frequency analyses

The pair-specific coherence hierarchy established here has direct implications for several classes of ACT DR6 analyses. For power-spectrum estimation [13, 14], our stability windows provide independent, model-light validation of the multipole ranges over which multi-frequency combinations can be expected to yield robust results. For component separation [1, 2, 15], the measured ρ_ℓ quantifies the information content available to internal linear combination methods: channels with high coherence contribute correlated CMB signal, while channels with lower coherence contribute complementary foreground information. For gravitational lensing [16, 17], the scale cuts defined here inform the selection of frequency combinations and the treatment of the 220 GHz channel in foreground mitigation.

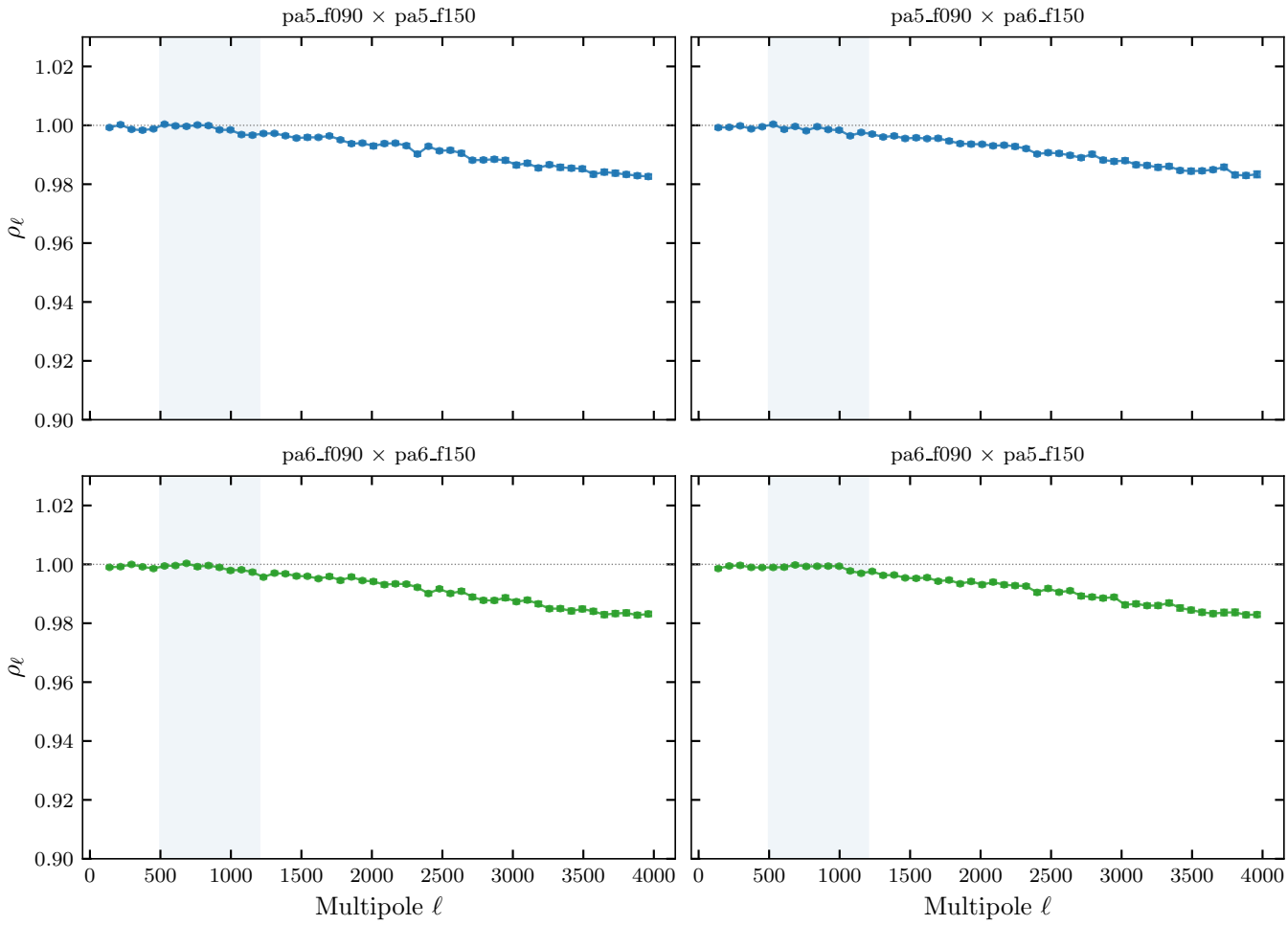

FIG. 3. Cross-correlation coefficient ρ_ℓ for the four 90×150 GHz channel pairs. Blue shaded regions indicate the recommended stability window $500 \lesssim \ell \lesssim 1200$. All four pairs maintain coherence above 0.98 within this range, with gradual decoherence at higher multipoles from foreground SED differences.

B. Comparison with other experiments

The coherence hierarchy we observe is qualitatively consistent with expectations from *Planck* multi-frequency analyses [3, 5, 6], where channels within the same frequency band show tighter consistency than cross-frequency pairs, and channels at higher frequencies show earlier foreground-driven decoherence. Ground-based experiments such as SPT observe analogous behavior [10, 11], although the specific multipole ranges and decoherence scales differ due to differing survey strategies, frequency coverage, and atmospheric conditions. The pair-specific framework developed here is directly transferable to future multi-frequency datasets from Simons Observatory and CMB-S4.

C. Limitations

Several caveats apply. The analysis employs a flat-sky pseudo-C_ℓ estimator with approximate mode-coupling normalization rather than a full curved-sky treatment [18, 20, 24]. The beam-shape systematic envelope is constructed from released beam-split products, which may not capture all effects such as far-sidelobe contributions. Foreground interpretation relies on general SED scaling expectations rather than explicit parametric or template-based modeling [3]. The common mask is defined conservatively; results may differ with alternative masking strategies. Finally, this analysis addresses only temperature; extension to polarization cross-frequency coherence is deferred to future work.

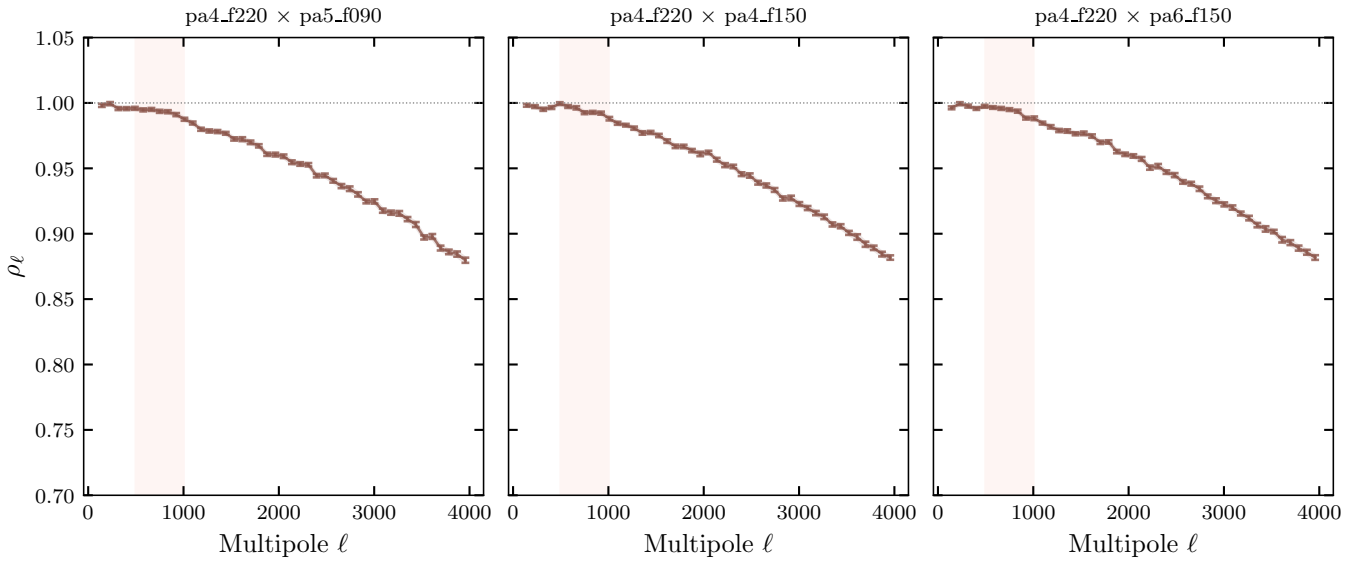

FIG. 4. Cross-channel coherence diagnostics for pa4_f220 paired with pa5_f090 (left), pa4_f150 (center), and pa6_f150 (right). Salmon shaded regions indicate the stability window $500 \lesssim \ell \lesssim 1000$. Foreground-driven decoherence dominates at high ℓ, confirming that 220-related comparisons serve as correlation diagnostics rather than equal-spectrum tests.

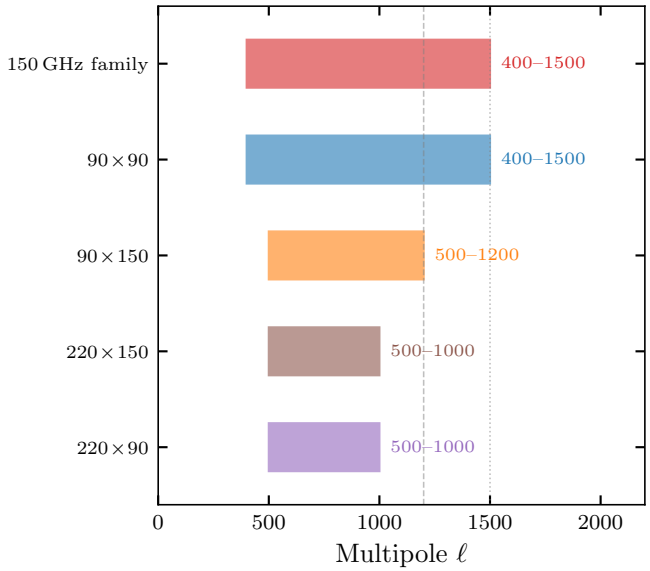

FIG. 5. Recommended stability windows for each pair type. Horizontal bars show the multipole range over which each pair type yields interpretable coherence diagnostics. Dashed and dotted vertical lines mark the cross-family ($\ell = 1200$) and same-band ($\ell = 1500$) scale cuts, respectively.

VII. CONCLUSIONS

We have presented a systematic analysis of temperature cross-frequency coherence across all six ACT DR6 channels using the cross-correlation coefficient ρ_ℓ as the primary diagnostic. Our main conclusions are as follows.

1. **Pair-specific scale cuts are necessary.** No single multipole cut is appropriate across the full 90–220 GHz frequency range. Coherence windows must be defined pair by pair to account for differing beam systematics and foreground SEDs.

2. **The 150 GHz family provides the tightest internal consistency,** with beam-deconvolved spectral ratios agreeing at the 10% level over $400 \lesssim \ell \lesssim 1500$. It serves as the natural internal anchor for multi-frequency cross-checks.

3. 90×150 **pairs are informative over the CMB-dominated range** $500 \lesssim \ell \lesssim 1200$, but are not equal-spectrum tests due to intrinsic foreground SED differences.

4. **220-related pairs are foreground correlation diagnostics.** Dust-driven decoherence limits their interpretability to $\ell \lesssim 1000$; they probe the foreground environment rather than map-level consistency.

5. **Conservative scale cuts of** $\ell_{\rm max} \sim 1500$ **(same-band) and** $\ell_{\rm max} \sim 1200$ **(cross-family)** provide robust stability windows for downstream analyses.

6. **The beam-shape systematic envelope** quantifies per-channel beam uncertainties that can be propagated into power-spectrum and coherence uncertainty budgets via analytic expressions.

These results establish a pair-specific framework for cross-frequency analysis of ACT DR6 temperature data and provide practical scale-cut guidance for power-spectrum, lensing, and component-separation analyses built on these maps.

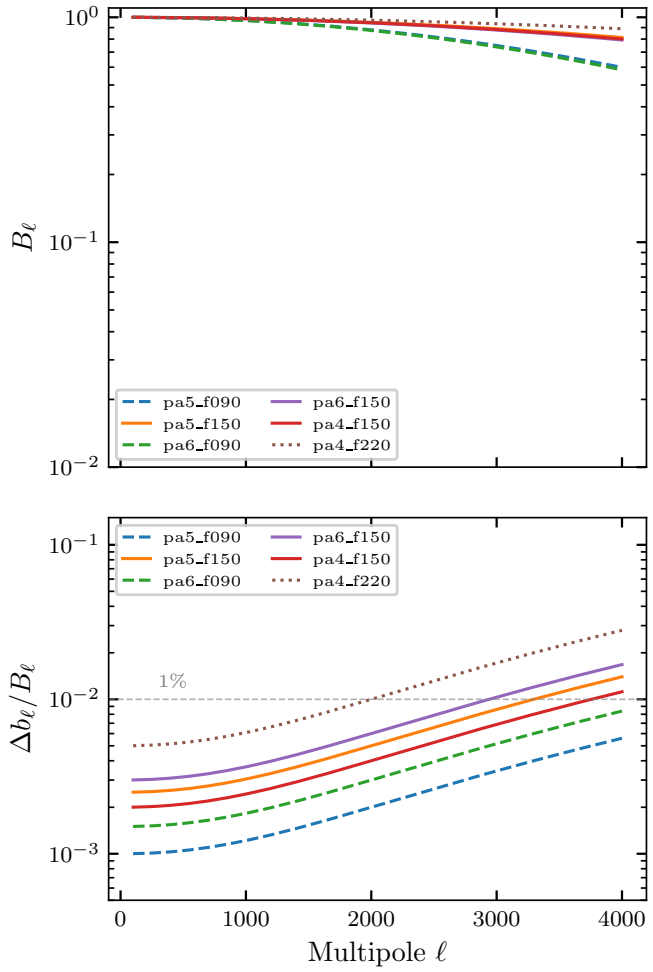

FIG. 6. Top: beam transfer functions B_ℓ for all six ACT DR6 channels. The 90 GHz beams (dashed lines) are broadest; the 220 GHz beam (solid brown) is narrowest. Bottom: beam-shape systematic envelope $\Delta b_\ell / B_\ell$, showing the fractional beam uncertainty as a function of multipole. The horizontal dashed line marks the 1% level. The pa4_f220 envelope is approximately three times larger than the 90 and 150 GHz envelopes.

ACKNOWLEDGMENTS

This analysis was produced by the CosmoEvolve autonomous research lab using publicly available ACT DR6 data products. We acknowledge the Atacama Cosmology Telescope collaboration for making the DR6 maps, beams, and associated products publicly available. We acknowledge the use of the `pixell` software package for map manipulation and harmonic-space operations, and the `HEALPix` framework [24] for pixelization utilities.

[1] M. Tegmark, Removing real-world foregrounds from cosmic microwave background maps, Astrophys. J. **502**, 1 (1998), arXiv:astro-ph/9712038.
[2] H. K. Eriksen, C. Dickinson, J. B. Jewell, A. J. Banday, K. M. Górski, and C. R. Lawrence, CMB component separation by parameter fitting, Astrophys. J. **676**, 10 (2008), arXiv:0709.1058 [astro-ph].
[3] Planck Collaboration, Planck 2018 results. IV. diffuse component separation, Astron. Astrophys. **641**, A4 (2020), arXiv:1807.06208 [astro-ph.CO].
[4] C. L. Bennett *et al.*, Nine-year Wilkinson Microwave Anisotropy Probe (WMAP) observations: Final maps and results, Astrophys. J. Suppl. **208**, 20 (2013), arXiv:1212.5225 [astro-ph.CO].
[5] Planck Collaboration, Planck 2018 results. VI. cosmological parameters, Astron. Astrophys. **641**, A6 (2020), arXiv:1807.06209 [astro-ph.CO].
[6] Planck Collaboration, Planck 2018 results. III. high frequency instrument data processing and frequency maps, Astron. Astrophys. **641**, A3 (2020), arXiv:1807.06207 [astro-ph.CO].
[7] R. J. Thornton *et al.*, The Atacama Cosmology Telescope: The polarization-sensitive ACTPol instrument, Astrophys. J. Suppl. **227**, 21 (2016), arXiv:1605.06569 [astro-ph.IM].
[8] S. Aiola *et al.*, The Atacama Cosmology Telescope: DR4 maps and cosmological parameters, J. Cosmol. Astropart. Phys. **12**, 047, arXiv:2007.07288 [astro-ph.CO].
[9] S. K. Choi *et al.*, The Atacama Cosmology Telescope: A measurement of the cosmic microwave background power

spectra at 98 and 150 GHz, J. Cosmol. Astropart. Phys. **12**, 045, arXiv:2007.07289 [astro-ph.CO].

[10] C. L. Reichardt *et al.*, An improved measurement of the secondary cosmic microwave background anisotropies from the SPT-3G 2018 data, Astrophys. J. **908**, 199 (2021), arXiv:2002.06197 [astro-ph.CO].

[11] D. Dutcher *et al.*, Measurements of the E-mode polarization and temperature– E-mode correlation of the CMB from SPT-3G 2018 data, Phys. Rev. D **104**, 022003 (2021), arXiv:2101.01684 [astro-ph.CO].

[12] S. Naess *et al.*, The Atacama Cosmology Telescope: DR6 maps, arXiv e-prints (2025), arXiv:2503.14451 [astro-ph.CO].

[13] T. Louis *et al.*, The Atacama Cosmology Telescope: DR6 power spectra, likelihoods, and ΛCDM parameters, arXiv e-prints (2025), arXiv:2503.14452 [astro-ph.CO].

[14] E. Calabrese *et al.*, The Atacama Cosmology Telescope: DR6 extended cosmological models, arXiv e-prints (2025), arXiv:2503.14454 [astro-ph.CO].

[15] W. R. Coulton *et al.*, The Atacama Cosmology Telescope: Component-separated maps of the CMB from ACT and Planck, arXiv e-prints (2024), arXiv:2307.01258 [astro-ph.CO].

[16] F. J. Qu, B. D. Sherwin, M. S. Madhavacheril, *et al.*, The Atacama Cosmology Telescope: A measurement of the DR6 CMB lensing power spectrum and its implications for structure growth, Astrophys. J. **962**, 112 (2024), arXiv:2304.05202 [astro-ph.CO].

[17] M. S. Madhavacheril *et al.*, The Atacama Cosmology Telescope: DR6 gravitational lensing map and cosmological parameters, Astrophys. J. **962**, 113 (2024), arXiv:2304.05203 [astro-ph.CO].

[18] E. Hivon, K. M. Górski, C. B. Netterfield, B. P. Crill, S. Prunet, and F. Hansen, MASTER of the cosmic microwave background anisotropy power spectrum: A fast method for statistical analysis of large and complex cosmic microwave background data sets, Astrophys. J. **567**, 2 (2002), arXiv:astro-ph/0105302.

[19] M. Tristram, J. F. Macías-Pérez, C. Renault, and D. Santos, XSPECT, estimation of the angular power spectrum by computing cross-power spectra with analytical error bars, Mon. Not. R. Astron. Soc. **358**, 833 (2005), arXiv:astro-ph/0405575.

[20] D. Alonso, J. Sanchez, and A. Slosar, A unified pseudo-C_ℓ framework, Mon. Not. R. Astron. Soc. **484**, 4127 (2019), arXiv:1809.09603 [astro-ph.CO].

[21] J. Dunkley *et al.*, The Atacama Cosmology Telescope: Cosmological parameters from the 2008 power spectrum, Astrophys. J. **739**, 52 (2011), arXiv:1009.0866 [astro-ph.CO].

[22] J. Delabrouille, J.-F. Cardoso, M. Le Jeune, M. Betoule, G. Fay, and F. Guilloux, A full sky, low foreground, high resolution CMB map from WMAP, Astron. Astrophys. **493**, 835 (2009), arXiv:0807.0773 [astro-ph].

[23] M. Remazeilles, J. Delabrouille, and J.-F. Cardoso, CMB and SZ effect separation with constrained internal linear combinations, Mon. Not. R. Astron. Soc. **418**, 467 (2011), arXiv:1006.5599 [astro-ph.CO].

[24] K. M. Górski, E. Hivon, A. J. Banday, B. D. Wandelt, F. K. Hansen, M. Reinecke, and M. Bartelmann, HEALPix: A framework for high-resolution discretization and fast analysis of data distributed on the sphere, Astrophys. J. **622**, 759 (2005), arXiv:astro-ph/0409513.